Original Article
Differentiating benign and malignant parotid gland tumors using CT images and machine learning algorithms

Yushuai Yuan[1,2*], Yue Hong[3*], Xiaoyi Lv[2,4,5], Jianming Peng[6], Min Li[2,4,5], Dong Guo[3], Pan Huang[1], Chen Chen[1,2], Ziwei Yan[1,2], Cheng Chen[1,2], Hongmei Li[7], Hongbing Ma[1,8], Yan Wang[3]

[1]College of Information Science and Engineering, Xinjiang University, Urumqi 830046, Xinjiang, China; [2]Key Laboratory of Signal Detection and Processing, Xinjiang University, Urumqi 830046, Xinjiang, China; [3]Radiology Center, People's Hospital of Xinjiang Uygur Autonomous Region, Urumqi 830001, Xinjiang, China; [4]College of Software, Xinjiang University, Urumqi 830046, Xinjiang, China; [5]Key Laboratory of Software Engineering Technology, Xinjiang University, Urumqi 830046, Xinjiang, China; [6]Information Department, People's Hospital of Xinjiang Uygur Autonomous Region, Urumqi 830001, Xinjiang, China; [7]College of Resources and Environmental Sciences, Xinjiang University, Urumqi 830046, Xinjiang, China; [8]Department of Electronic Engineering, Tsinghua University, Beijing 100084, China. *Equal contributors.

Abstract: Correctly diagnosing parotid gland tumors before surgery is of great significance for clinicians formulating surgical plans, as they are related to patient prognosis. This study evaluated the value of computed tomography (CT) images combined with machine learning algorithms in the differential diagnosis of benign tumors and malignant tumors (BTs and MTs) of the parotid gland. A total of 177 CT images of parotid gland tumors were analyzed in this study, including 99 BT images and 78 MT images. First, the morphological and textural features of the tumor area were extracted, then the least absolute shrinkage and selection operator (Lasso) algorithm was used to reduce the dimensionality of the serially fused features, and finally, the support vector machine (SVM) algorithm was selected to build a classification model. The area under the receiver operating characteristic curve (AUC) was used for the model evaluation. The experimental results demonstrated that the accuracy of the SVM model based on the genetic algorithm (GA-SVM) reached 85.42%, the sensitivity was 72.73%, the specificity was 92.97%, and the AUC was 0.8821. The diagnostic model we proposed could assist doctors in preoperative, noninvasive differential diagnoses, which can better guide the clinical treatment selection.

Keywords: Parotid gland tumors, computed tomography images, machine learning algorithms, differential diagnosis

Introduction

Salivary gland tumors are the most common disease in salivary gland tissue and account for approximately 0.5% of all malignant tumors (MTs) [1, 2]. Among all salivary gland tumors, parotid gland tumors have the highest incidence, accounting for approximately 80%, of which approximately 75% are benign tumors (BTs), and the rest are MTs that threaten patients' survival and quality of life [3, 4]. In fact, BTs are treated with limited surgery, and the incidence of complications is low, while MTs require more aggressive surgery [5]. Be-

cause the choice of treatment depends on the tumor's histological type, differentiating BTs and MTs of the parotid gland is particularly important for correct, appropriate, and timely treatment [6].

Fine-needle aspiration cytology is considered to be the most accurate tool for distinguishing BTs and MTs of the parotid gland [7]. However, this invasive surgery may cause pain and complications such as increased tumor cell proliferation [8]. Therefore, radiological assessment plays an important role in this situation and can determine the nature of parotid gland

Table 1. Details of the parotid tumor patients (n=99)

Characteristic	BTs	MTs
Sex	56	43
Male	37	25
Female	19	18
Age	52.6 ± 14.8	53.3 ± 15.5

Note: Except for age (mean ± SD), the values are the number of patients.

lesions using a noninvasive method [6]. At present, the common imaging methods for evaluating parotid gland tumors are ultrasonography (US), magnetic resonance imaging (MRI), and computed tomography (CT) [9-11].

There are many studies on the identification of parotid gland tumors using US [12-14]. However, due to the sound shadow of the mandible, US has certain limitations for locating parotid gland tumors. In addition, it is easily affected by the operators. MRI is considered to be a good option for the evaluation of parotid tumors, because it can accurately assess the extent of the infiltration and the tumor demarcation. Some studies report that MRI can help clinicians make differential diagnoses of parotid tumors [15]. However, it has the disadvantages of limited availability, long scanning times, and high cost [16]. CT scans can clearly show the parotid gland border outline and the internal structure, especially after enhancement [17]. CT examination can also accurately locate parotid gland masses and can show the number of masses, the size, shape, and boundary of each mass, and the infiltration of the masses into the surrounding tissue. Therefore, CT can be used to differentiate BTs and MTs of the parotid gland and is of great value in determining the surgical plan and the method of further treatment [17]. In addition, CT is an economical and highly prevalent imaging examination method and is the first choice for many patients. Therefore, CT images of the parotid gland tumor were selected as our research focus.

In recent years, many research institutes have carried out studies on the differential diagnosis of parotid gland tumors based on medical imaging. Lin Li et al. [16] evaluated the value of single-source dual-energy computed tomography (ssDECT) in the differentiation of BTs and MTs of the parotid gland. When the iodine concentration (IC) was set to 0.91 mg/mL, the accuracy rate for distinguishing polymorphic adenomas (PAs) from MTs was 94.2%. Ajmi et al. [18] combined DECT texture analysis with the random forest (RF) method to distinguish the two main BTs of the parotid gland (Warthin tumors and PAs). The classification accuracy, sensitivity, and specificity on independent test sets reached 92%, 86%, and 100%, respectively. Kato et al. [19] evaluated the performance of CT and MRI of parotid gland tumors and found that the imaging features of cystic components in the tumor were useful for the differential diagnosis of BTs and MTs of the parotid gland. Another study [20] retrospectively analyzed the diagnostic performance of three radiologists with different experience levels in assessing the CT and MRI of salivary gland tumors. The results showed that the diagnostic accuracy of the assessment of salivary gland tumors largely depends on the experience of radiologists, and the diagnostic accuracy improves as the doctor's experience increases. Disease diagnosis is one of the more labor-intensive tasks in the medical system. The introduction of machine learning algorithms can not only greatly reduce labor costs but also obtain more objective diagnostic results in real time. However, at present, there is no radiological research using enhanced CT image features combined with pattern recognition algorithms to classify BTs and MTs of the parotid gland. Therefore, this study evaluated the value of CT images combined with machine learning algorithms in the differential diagnosis of parotid gland tumors, and we propose a support vector machine (SVM) classification model based on the least absolute shrinkage and selection operator (Lasso) algorithm that can assist doctors in their preoperative, noninvasive differential diagnosis and provide a basis for clinical decision making.

Materials and methods

Experimental data set

This study included 99 parotid tumor patients (including 56 BTs and 43 MTs) with preoperative CT as a data set from People's Hospital of Xinjiang Uygur Autonomous Region from October 2009 to July 2018. The details of the patient characteristics are shown in **Table 1**.

To improve the generalization ability of the diagnostic model, we selected an average of 2 cross-sectional images of portal vein-enhanced CT with a larger tumor area from the CT sequence of each patient [21, 22]. Finally, 99 CT images of BTs and 78 CT images of MTs were selected. All the procedures performed in the studies involving human participants were carried out in accordance with the ethical standards of the Ethics Review Committee of the People's Hospital of Xinjiang Uygur Autonomous Region. The study was done after documenting the patients' informed consent.

CT protocol

All the scans were performed using a GE Light Speed VCT 64 row CT Scanner with the following scanning parameters: the tube voltage was 100-120 kV, the tube current was 250-300 mA, the tube speed was 0.4 s/r, the pitch was 0.531/0.969, the matrix was 512×512, the field of view was 18-24 cm, and the scanning layer thickness was 5 mm. The patient was placed in a supine position, and the axial scan ranged from the external auditory canal to the lower thyroid edge. A flat scan was used to determine the scope and maximum area of the lesion. Sixty milliliters of nonionic contrast agent (Onepac 300 mg/ml) was injected via the cubital vein at a flow rate of 4 ml/s.

Experimental process

Our experimental process is shown in **Figure 1** and consists of the following parts that are processed consecutively: 1) Parotid tumor segmentation, 2) Feature extraction and selection, 3) Classifier design and evaluation. In the following sections, we will expand on the details.

ROI segmentation

First, the CT images in the Digital Imaging and Communications in Medicine (DICOM) format were converted to the Joint Photographic Experts Group (JPEG) format. For medical images, the region of interest (ROI) refers to the part of the image that the doctor believes is most meaningful for diagnosis. It has been reported that the dice similarity coefficient (DSC) of automatic parotid gland segmentation has reached 0.9226 [23]. Therefore, there is still over-segmentation or under-segmenta-

tion in automatic parotid gland segmentation, and there is still a certain deviation from the doctor's standard. If the segmentation result is not ideal, it will directly affect the subsequent classification accuracy. To better identify BTs and MTs of the parotid gland, this study used artificial methods to segment parotid gland tumors. A radiologist with more than five years of experience manually drew the ROI along the tumor edge in each visualized tumor image on the labeled software, and the segmentation results were reviewed by another senior radiologist. The segmentation flow chart is shown in **Figure 2**.

Feature extraction

In this study, a total of 194 features (as shown in **Table 2**) were extracted from the ROIs of the CT images, including (1) 8 morphological features, which were used to quantify the physician's subjective morphological observation results, (2) 26 texture features, including 4 features based on gray level difference statistics (GLDS), 15 features based on the gray level gradient co-occurrence matrix (GLGCM), and 7 features based on the gray level run length matrix (GLRLM), and (3) 160 wavelet transform features.

Feature fusion and selection

In this study, the 194 features were fused together through serial fusion. However, not all the extracted features contribute to the training of the classification model, so removing these redundant features can ensure the accuracy while reducing the complexity of the model, thereby reducing wasted time and resources [24]. In this study, the Lasso algorithm was used for feature selection.

The Lasso algorithm searches for the optimal feature subset and evaluates the feature subset according to the classification effect [25]. Its equation is shown in equation (1). The Lasso algorithm is very suitable for the dimensionality reduction of data. Its advantage is that the weights of some unimportant variables in the model are directly compressed to zero so that the model is simplified.

$$min_w \sum_{i=1}^{m} (y_i - w^T x_i)^2 + \lambda \parallel w \parallel_1 \qquad (1)$$
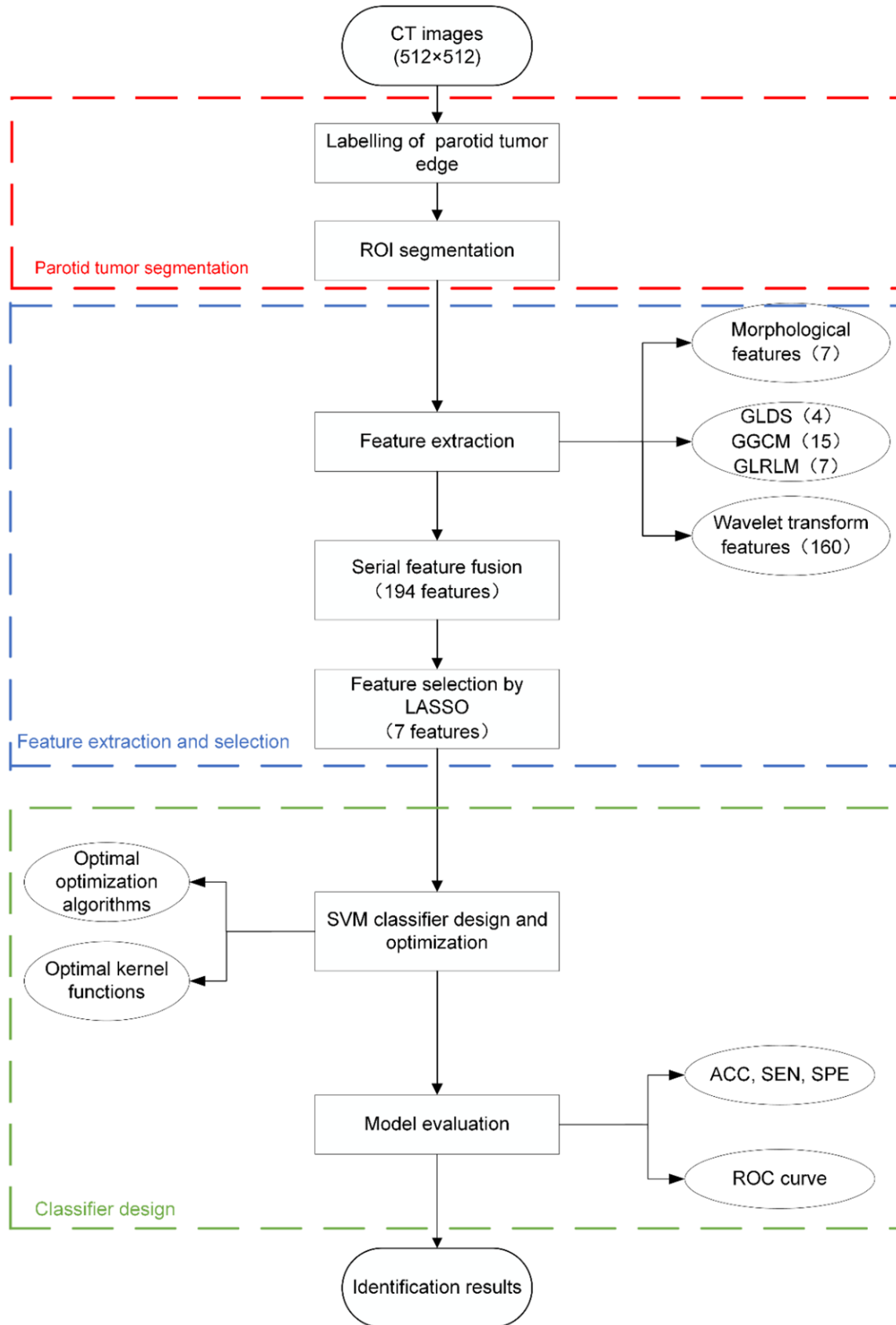
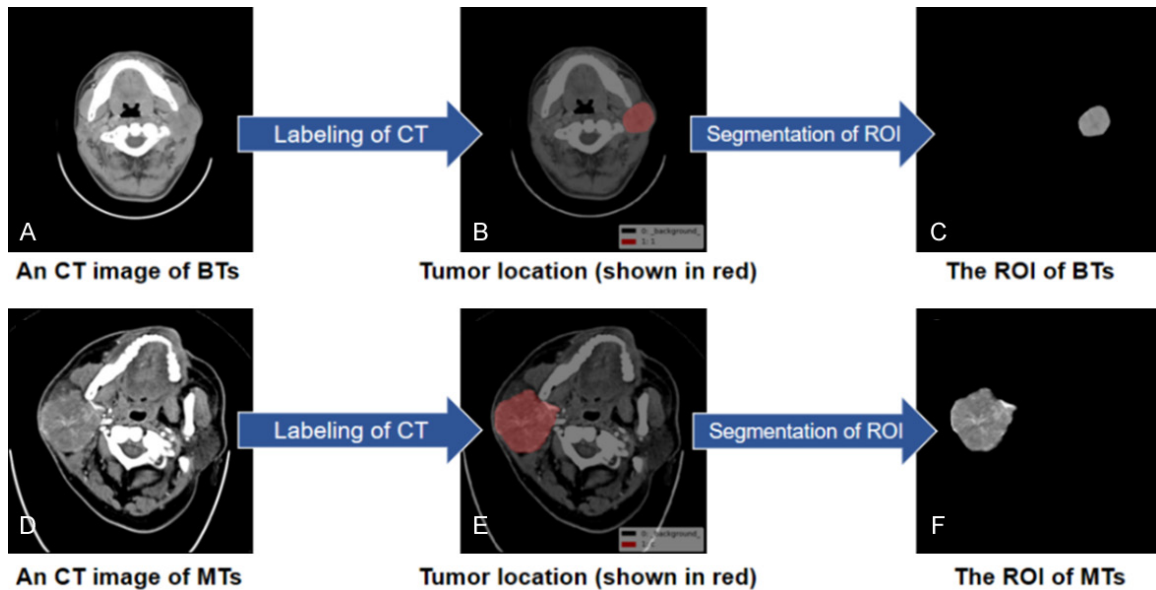**Figure 1.** A flowchart of the proposed identification model.

Figure 2. Flow diagram of ROI segmentation. (A) is the CT image of a 19-year-old man with pleomorphic adenoma on the left, and (D) is the CT image of a 49-year-old man with a malignant parotid gland tumor on the right; (B and E) show the locations of the parotid gland tumors in the original CT images as shown in red; (C and F) are the ROIs of the parotid CT images after segmentation.

Table 2. Statistics of the multidomain features

Method	Feature name	Total number
Morphological features	Height, width, perimeter, area, complexity, rectangularity, elongation, equivalent area radius	8
GLDS	Mean, contrast, angular second moment, entropy	4
GLGCM	Small grads dominance, big grads dominance, gray asymmetry, grads asymmetry, energy, gray mean, grads mean, gray variance, grads variance, correlation, gray entropy, grads entropy, entropy, inertia, differ moment	15
GLRLM	Short run emphasis, long run emphasis, gray-level nonuniformity, run percentage, run-length nonuniformity, low gray-level run emphasis, high-gray level run emphasis	7
Wavelet transform		160
Total		194

Design and optimization of the SVM classifier

SVM is a machine learning method based on the statistical learning theory proposed by Cortes and Vapnik [26]. SVM is a supervised learning algorithm, and its learning strategy is to maximize the classification interval. SVM is a very common method in pattern recognition, and it has many unique advantages for small samples and nonlinear and high-dimensional pattern recognition.

The choice of kernel function will affect the classification performance of SVM. The commonly used kernel functions of SVM are linear kernel, polynomial kernel, Radial Basis Functions (RBF), and sigmoid kernel. In addition, this study also introduced three commonly used optimization algorithms: the grid search (GS) algorithm, the particle swarm optimiza-tion (PSO) algorithm and the genetic algorithm (GA). We found a suitable optimization algorithm and a kernel function through many experiments.

Model evaluation

To better evaluate our proposed model, this study uses the specificity, sensitivity, accuracy and receiver operating characteristic (ROC) curve to judge the performance of the classifier and uses the area under the ROC curve (AUC) to quantify the generalization ability of the model. The definitions of specificity, sensitivity, and accuracy are as follows:

$$\text{Sensitivity} = \frac{TP}{TP + FN} \qquad (2)$$

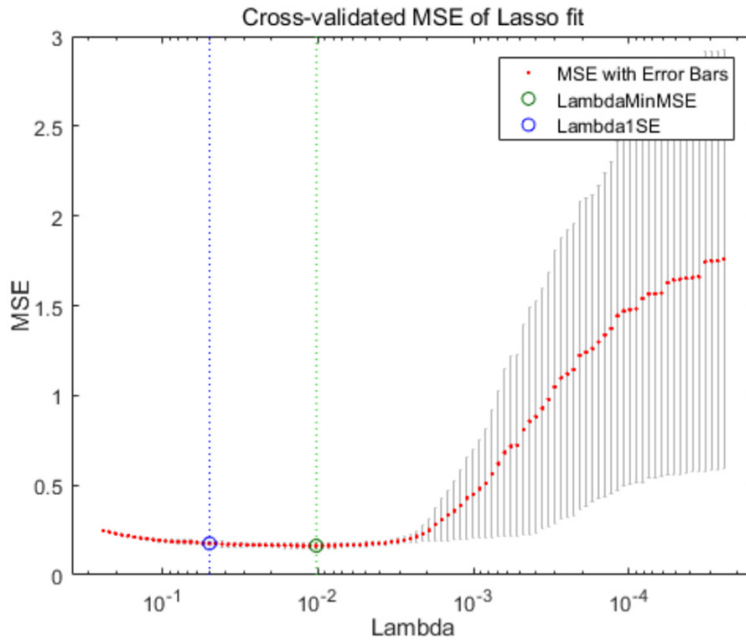$$\text{Specificity} = \frac{TN}{TN + FP} \qquad (3)$$

Figure 3. A 10-fold CV of the Lasso feature selection.

Table 3. The average ACC, SEN, SPE and time with different feature selection methods

Method	Features	ACC (%)	SEN (%)	SPE (%)	Time (s)
Original	194	69.49	54.55	78.38	144.16
Lasso	7	85.42	72.73	92.97	30.55

$$\text{Accuracy} = \frac{TP + TN}{TP + FN + TN + FP} \quad (4)$$

TP, FP, FN, and TN represent true positive, false positive, false negative, and true negative samples, respectively. Positive represents patients with malignant tumors of the parotid gland, and negative represents patients with benign tumors of the parotid gland.

We also calculated the horizontal and vertical axes of the ROC curve, where the horizontal axis is the false positive rate (FPR) and the vertical axis is the true positive rate (TPR), defined as equation (5) and equation (6), respectively.

$$FPR = \frac{FP}{TN + FP} \quad (5)$$

$$TPR = \frac{TP}{TP + FN} \quad (6)$$

Results

The statistical analysis component of this study was carried out with MATLAB R2016a software, in which an SVM discriminant analysis was implemented using the LIBSVM toolbox created by Lin and Chang [27]. All the experimental results were taken as the average of 5 experiments.

Results and comparison of the feature selection

The larger the λ value of the Lasso algorithm is, the sparser the solution of the parameters and the fewer the number of features selected. Therefore, 10-fold cross-validation (CV) was used to evaluate the reliability of the Lasso algorithm. By calculating the mean square error (MSE) of the model, the minimum point of MSE was selected, as shown in **Figure 3**. Finally, 7 features were selected to build a classifier model.

This study also compared the accuracy of the Lasso algorithm with the method without feature selection, as shown in **Table 3**. **Table 3** shows that the Lasso algorithm greatly reduces the dimensionality of the data. On the premise of ensuring the classification accuracy, the average optimization time was reduced by 113.61 s compared with no feature selection, thus verifying the reasonableness of the Lasso algorithm used in this study.

SVM classifier results

In the SVM model, the GS algorithm, the PSO algorithm, and GA were used to optimize the penalty parameter C and Gaussian width g. The key parameters are shown in **Table 4**. We further compared the classification performance of the different optimization algorithm models under the four kernel functions, as shown in **Table 5**. The experiment used a 5-fold CV method. It can be seen from **Table 5** that GA-RBF-SVM has achieved the best results, with the highest accuracy rate of 85.42%, which also verified the rationality of choosing GA and RBF in this study.

Table 4. The key parameters of GS-SVM, PSO-SVM, and GA-SVM

Classifier	Parameter	Parameter value	Parameter	Parameter value
GS-SVM	Range of C	$[2^{-8}, 2^8]$	Range of g	$[2^{-8}, 2^8]$
	Step length of C	0.3	Step length of g	0.3
PSO-SVM	Range of C	$[10^{-1}, 10^2]$	Range of g	$[10^{-2}, 10^3]$
	Local search capability	1.5	Global search capability	1.7
	Maximum number of generations	100	Maximum number of population	20
GA-SVM	Range of C	$[0, 10^2]$	Range of g	$[0, 10^3]$
	Maximum number of generations	300	Maximum number of population	60
	Generation gap	0.9		

Table 5. The average test/training accuracy and time with different kernel functions and optimization algorithms

Classifier	Kernel function	Test/training accuracy (%)	Time (s)
GS-SVM	Linear kernel	76.27/86.44	7.04
	Polynomial kernel	83.05/93.22	7.03
	RBF	81.36/92.37	7.12
	Sigmoid kernel	62.71/52.54	7.15
PSO-SVM	Linear kernel	72.20/80.17	9.36
	Polynomial kernel	78.64/86.27	9.23
	RBF	84.75/98.14	9.33
	Sigmoid kernel	62.71/52.54	9.18
GA-SVM	Linear kernel	73.22/80.85	26.72
	Polynomial kernel	79.32/90.85	28.38
	RBF	85.42/98.64	30.55
	Sigmoid kernel	62.71/52.54	26.04

Table 6. The average ACC, SEN, and SPE with the different algorithms

	ACC (%)	SEN (%)	SPE (%)
GS-SVM	83.05	68.18	91.89
PSO-SVM	84.75	72.73	91.89
GA-SVM	85.42	72.73	92.97
KNN	71.52	57.27	91.89
BPNN	73.56	46.36	89.73

Comparison of the diagnostic models

In this study, the commonly used machine learning algorithms K-Nearest Neighbor (KNN), Back Propagation Neural Network (BPNN) and the best results of SVM under three optimization algorithms were compared, as shown in **Table 6**. The key parameters of the KNN and BPNN algorithms are shown in **Table 7**. As seen in **Table 6**, the GA-SVM model has the

best performance among the five methods, with an average accuracy of 85.42%, an average sensitivity of 72.73%, and an average specificity of 92.97%. In comparing the results with those of the other four models, the GA-SVM model was found to be more reliable.

In addition, we also plotted the ROC curves of GS-SVM, PSO-SVM, GA-SVM, KNN, and BPNN and calculated their corresponding AUC values, as shown in **Figure 4** and **Table 8**, respectively. As seen in **Table 8**, the AUC value of GA-SVM was the highest, reaching 0.8821. The experimental results showed that our proposed GA-SVM model has a better classification accuracy and a generalization ability than KNN and BPNN.

Discussion

As the surgical and treatment plans for benign and malignant tumors of the parotid gland are different, the accurate preoperative diagnosis of parotid gland tumors is very important [28]. In order to eliminate the interference of non-lesion areas on the classification of benign and malignant tumors, we first segmented the CT images of the parotid gland tumors and extracted the tumor lesion areas. Feature extraction is crucial for machine learning algorithms, which means that features and data determine the upper limit of the algorithm [29]. According to earlier studies, textural features such as GLDS, GLGCM, and GLRLM are now widely used in the classification of CT images of pancreatic cancer [30, 31]. Li et al. [30] extracted 202-dimensional features including texture features from CT images of pancreatic cancer, and proposed a model for the preoperative diagnosis and staging of pancreatic cancer based on an ensemble learning-support

Table 7. The key parameters of KNN and BPNN

Classifier	Parameter	Parameter value	Parameter	Parameter value
KNN	Number of neighbors	5	Distance metric	Euclidean
	Distance weight	Equal	Standardize data	True
BPNN	Maximal iteration times	2000	Target error	0.00001
	Display interval	500	Learning rate	0.05
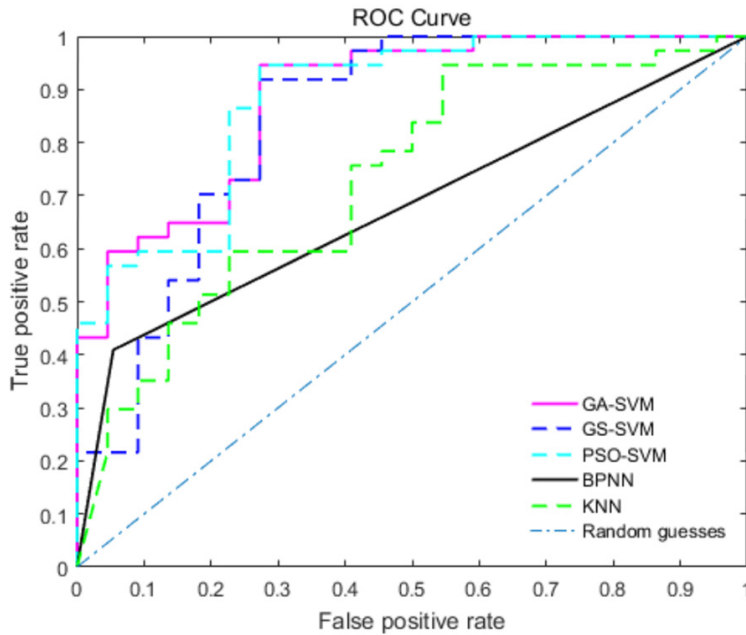
Figure 4. ROC curves of the five algorithms.

Table 8. The AUC values of the five algorithms

	GS-SVM	PSO-SVM	GA-SVM	KNN	BPNN
AUC value	0.8440	0.8808	0.8821	0.7297	0.6775

GA and PSO algorithms are both bionic algorithms. The PSO algorithm mainly simulates social behaviors such as bird foraging and human cognition, and GA mainly borrows the law of survival of the fittest in biological evolution [33]. In GA optimization, chromosomes share information with each other, so the entire population moves more evenly to the optimal area [34]. However, the particles in the PSO algorithm only share information through the current search to the best point [35]. To a large extent, this is a single information sharing mechanism. The entire search and update process follows the current optimal solution process. This may be the reason why GA-SVM is more accurate than PSO-SVM in our experiments. At the same time, this also causes the convergence speed of the PSO algorithm to be faster than the convergence speed of the GA. It can be seen from **Tables 6** and **7** that the accuracy and stability of SVM are better than those of KNN and BPNN, which shows that SVM performs better in the face of small sample problems in the medical field, and it is easier to mine the nonlinear relationship between data and features [36-38].

vector machine. Considering that both the parotid gland and the pancreas belong to the glandular tissue of the human body, we tried to apply these texture features to the classification of CT images of parotid gland tumors. In addition, in the diagnosis of parotid gland tumors, the doctor's subjective observation of the parotid gland tumor is also very important, so we also added morphological features [32]. It can be seen from **Tables 5** and **6** that these features play a positive role in the classification of parotid benign and malignant tumors. Then we used the Lasso algorithm for feature selection to reduce the dimensionality of the data while ensuring the classification accuracy.

As seen in **Table 5**, GA has a better optimization effect on SVM than the PSO algorithm. The

Conclusion

This paper is the first to study the classification of BTs and MTs of the parotid gland with CT and machine learning algorithms, and we proposed a differential diagnosis model of parotid gland tumors based on enhanced-CT images and the SVM algorithm. In this study, we first extracted 194 image features from the CT images of patients with parotid gland tumors and then

used the Lasso model to screen out 7 features that can efficiently distinguish benign tumors from malignant tumors. Finally, we used a variety of classification algorithms to construct a classification model and performed a comparative analysis. The average AUC value of the GA-SVM model reached 0.8821, which showed that the model we proposed has a good reliability and a certain practicality. The research results can assist doctors in preoperative and noninvasive differential diagnosis, thereby reducing the workload of doctors and providing a basis for clinical decision making.

Acknowledgements

Disclosure of conflict of interest

None.

Address correspondence to: Hongbing Ma, College of Information Science and Engineering, Xinjiang University, 666 Shengli Road, Urumqi 830046, Xinjiang, China. E-mail: mahongbing01@163.com; Yan Wang, Radiology Center, People's Hospital of Xinjiang Uygur Autonomous Region, 91 Tianchi Road, Urumqi 830001, Xinjiang, China. E-mail: drwangxj@sina.cn

References

[1] Carlson ER. Management of parotid tumors. J Oral Maxillofac Surg 2017; 75: 247-248.

[2] Ho K, Lin H, Ann DK, Chu PG and Yen Y. An overview of the rare parotid gland cancer. Head Neck Oncol 2011; 3: 40.

[3] Pinkston JA and Cole P. Incidence rates of salivary gland tumors: results from a population-based study. Otolaryngol Head Neck Surg 1999; 120: 834-840.

[4] Roh JL, Ryu CH, Choi SH, Kim JS, Lee JH, Cho KJ, Nam SY and Kim SY. Clinical utility of F-18-FDG PET for patients with salivary gland malignancies. J Nucl Med 2007; 48: 240-246.

[5] Magnano M, Gervasio CF, Cravero L, Machetta G, Lerda W, Beltramo G, Orecchia R, Ragona R and Bussi M. Treatment of malignant neoplasms of the parotid gland. Otolaryngol Head Neck Surg 1999; 121: 627-632.

[6] Christe A, Waldherr C, Hallett R, Zbaeren P and Thoeny H. MR imaging of parotid tumors: typical lesion characteristics in mr imaging improve discrimination between benign and ma-

[7] lignant disease. AJNR Am J Neuroradiol 2011; 32: 1202-1207.

[7] Bhatia KS, Rasalkar DD, Lee YP, Wong KT, King AD, Yuen HY and Ahuja AT. Evaluation of real-time qualitative sonoelastography of focal lesions in the parotid and submandibular glands: applications and limitations. Eur Radiol 2010; 20: 1958-1964.

[8] Kaya G and Howlett DC. The diagnosis of parotid lesions. Eur Radiol 2015; 25: 3025-3026.

[9] Bialek EJ, Jakubowski W, Zajkowski P, Szopinski KT and Osmolski A. US of the major salivary glands: anatomy and spatial relationships, pathologic conditions, and pitfalls. Radiographics 2006; 26: 745-764.

[10] Yabuuchi H, Fukuya T, Taijima T, Hachitanda Y, Tomita K and Koga M. Salivary gland tumors: diagnostic value of gadolinium-enhanced dynamic MR imaging with histopathologic correlation. Radiology 2003; 226: 345-354.

[11] Yerli H, Aydin E, Coskun M, Geyik E, Ozluoglu LN, Haberal N and Kaskati T. Dynamic multislice computed tomography findings for parotid gland tumors. J Comput Assist Tomogr 2007; 31: 309-316.

[12] Bialek EJ, Jakubowski W and Karpinska G. Role of ultrasonography in diagnosis and differentiation of pleomorphic adenomas - work in progress. Arch Otolaryngol Head Neck Surg 2003; 129: 929-933.

[13] Mansour N, Stock KF, Chaker A, Bas M and Knopf A. Evaluation of parotid gland lesions with standard ultrasound, color duplex sonography, sonoelastography, and acoustic radiation force impulse imaging - a pilot study. Ultraschall Med 2012; 33: 283-288.

[14] Shimizu M, Ussmuller J, Hartwein J, Donath K and Kinukawa N. Statistical study for sonographic differential diagnosis of tumorous lesions in the parotid gland. Oral Surg Oral Med Oral Pathol Oral Radiol Endod 1999; 88: 226-233.

[15] Gokce E. Multiparametric magnetic resonance imaging for the diagnosis and differential diagnosis of parotid gland tumors. J Magn Reson Imaging 2020; 52: 11-32.

[16] Li L, Zhao YF, Luo DH, Yang L, Hu L, Zhao XM, Wang Y and Liu WS. Diagnostic value of single-source dual-energy spectral computed tomography in differentiating parotid gland tumors: initial results. Quant Imaging Med Surg 2018; 8: 588-596.

[17] Burke CJ, Thomas RH and Howlett D. Imaging the major salivary glands. Br J Oral Maxillofac Surg 2011; 49: 261-269.

[18] Al Ajmi E, Forghani B, Reinhold C, Bayat M and Forghani R. Spectral multi-energy CT texture analysis with machine learning for tissue clas-

sification: an investigation using classification of benign parotid tumours as a testing paradigm. Eur Radiol 2018; 28: 2604-2611.

[19] Kato H, Kanematsu M, Watanabe H, Mizuta K and Aoki M. Salivary gland tumors of the parotid gland: CT and MR imaging findings with emphasis on intratumoral cystic components. Neuroradiology 2014; 56: 789-795.

[20] Vogl TJ, Albrecht MH, Nour-Eldin NA, Ackermann H, Maataoui A, Stöver T, Bickford MW and Stark-Paulsen T. Assessment of salivary gland tumors using MRI and CT: impact of experience on diagnostic accuracy. Radiol Med 2018; 123: 105-116.

[21] He M, Liu ZY, Lin YS, Wan JZ, Li J, Xu K, Wang Y, Jin ZY, Tian J and Xue HD. Differentiation of atypical non-functional pancreatic neuroendocrine tumor and pancreatic ductal adenocarcinoma using CT based radiomics. Eur J Radiol 2019; 117: 102-111.

[22] Pandey S, Singh PR and Tian J. An image augmentation approach using two-stage generative adversarial network for nuclei image segmentation. Biomed Signal Process Control 2020; 57: 101782.

[23] Zhong T, Huang X, Tang F, Liang SJ, Deng XG and Zhang Y. Boosting-based cascaded convolutional neural networks for the segmentation of CT organs-at-risk in nasopharyngeal carcinoma. Med Phys 2019; 46: 5602-5611.

[24] Chen C, Du GL, Tong DN, Lv GD, Lv XY, Si RM, Tang J, Li HY, Ma HB and Mo JQ. Exploration research on the fusion of multimodal spectrum technology to improve performance of rapid diagnosis scheme for thyroid dysfunction. J Biophotonics 2020; 13: 201900099.

[25] Zhang HQ, Wang J, Sun ZQ, Zurada JM and Pal NR. Feature selection for neural networks using group lasso regularization. IEEE Trans Knowl Data Eng 2020; 32: 659-673.

[26] Vapnik VN. An overview of statistical learning theory. IEEE Trans Neural Netw 1999; 10: 988-999.

[27] Chang CC and Lin CJ. LIBSVM: a library for support vector machines. ACM Trans Intell Syst Technol 2011; 2.

[28] Omura S, Kawata R, Higashino M, Nishikawa S, Terada T, Haginomori SI, Kurisu Y and Hirose Y. Challenges with preoperative diagnosis of low/intermediate-grade carcinoma of the parotid gland: single-center study of 112 patients. Eur Arch Otorhinolaryngol 2020; 277: 2031-2039.

[29] Lu ZC, Ma D and Liu LL. Identification of human diseases of the lower limbs based on medical infrared imaging and a CNN-LM model. Int J Clin Exp Med 2020; 13: 1379-1388.

[30] Li M, Nie X, Reheman Y, Huang P, Zhang S, Yuan Y, Chen C, Yan Z, Chen C, Lv X and Han W. Computer-aided diagnosis and staging of pancreatic cancer based on CT images. IEEE Access 2020; 8: 141705-141718.

[31] Zhang Y, Cheng C, Liu Z, Wang L, Pan G, Sun G, Chang Y, Zuo C and Yang X. Radiomics analysis for the differentiation of autoimmune pancreatitis and pancreatic ductal adenocarcinoma in F-18-FDG PET/CT. Med Phys 2019; 46: 4520-4530.

[32] Speight PM and Barrett AW. Salivary gland tumours. Oral Dis 2002; 8: 229-240.

[33] Chen C, Yang L, Li H, Chen F, Chen C, Gao R, Lv XY and Tang J. Raman spectroscopy combined with multiple algorithms for analysis and rapid screening of chronic renal failure. Photodiagnosis Photodyn Ther 2020; 30: 101792.

[34] Ma D, Lu ZEH, Liu LL and Lu XY. Infrared thermal imaging analysis of the human abdomen based on convolution neural network optimized by a genetic algorithm. Int J Clin Exp Med 2019; 12: 13288-13297.

[35] Lin SW, Ying KC, Chen SC and Lee ZJ. Particle swarm optimization for parameter determination and feature selection of support vector machines. Expert Syst Appl 2008; 35: 1817-1824.

[36] Tong D, Chen C, Zhang J, Lv G, Zheng X, Zhang Z and Lv X. Application of Raman spectroscopy in the detection of hepatitis B virus infection. Photodiagnosis Photodyn Ther 2019; 28: 248-252.

[37] Xie X, Chen C, Sun T, Mamati G, Wan X, Zhang W, Gao R, Chen F, Wu W, Fan Y, Lv X and Wu G. Rapid, non-invasive screening of keratitis based on Raman spectroscopy combined with multivariate statistical analysis. Photodiagnosis Photodyn Ther 2020; 31: 101932.

[38] Zheng C, Qing S, Wang J, Lu G, Li H, Lu X, Ma C, Tang J and Yue X. Diagnosis of cervical squamous cell carcinoma and cervical adenocarcinoma based on Raman spectroscopy and support vector machine. Photodiagnosis Photodyn Ther 2019; 27: 156-161.